Vol. 22, e220007 (2025)
doi: 10.2142/biophysico.bppb-v22.0007

Biophysics and Physicobiology
https://www.jstage.jst.go.jp/browse/biophysico/

Method and Protocol

Time-resolved small-angle X-ray scattering system development for the biological macromolecules at SACLA: A pilot study

Nobutaka Shimizu[1,2], Fangjia Luo[3], Tomoyuki Tanaka[4], Kensuke Tono[1,3], Keiko Yatabe[2], So Iwata[4], Eriko Nango[1,5]

[1]*RIKEN SPring-8 Center, Sayo, Hyogo 679-5148, Japan*
[2]*Photon Factory, Institute of Materials Structure Science, High Energy Accelerator Research Organization (KEK), Tsukuba, Ibaraki 305-0801, Japan*
[3]*Japan Synchrotron Radiation Research Institute, Sayo, Hyogo 679-5198, Japan*
[4]*Department of Cell Biology, Graduate School of Medicine, Kyoto University, Kyoto 606-8501, Japan*
[5]*Institute of Multidisciplinary Research for Advanced Materials, Tohoku University, Sendai, Miyagi 980-8577, Japan*

Received October 23, 2024; Accepted March 25, 2025;
Released online in J-STAGE as advance publication March 27, 2025
Edited by Haruki Nakamura

A time-resolved small-angle X-ray scattering (SAXS) system for protein solution samples using an X-ray free-electron laser (XFEL) was established by developing a SAXS diffractometer by integrating a helium path into the DAPHNIS system initially designed for Serial Femtosecond Crystallography (SFX) experiments at BL2 of SACLA. This modification enabled us to successfully capture the SAXS profiles of ovalbumin under conditions without any reaction trigger, using both the newly developed system and the sample solution flow device that was originally designed for SFX experiments. Furthermore, we conducted acid denaturation experiments on cytochrome c, using a T-junction-type solution mixing flow system, and observed the denaturation-induced changes in the SAXS profiles.

Keywords: BioSAXS, time-resolved measurement, solution X-ray scattering, XFEL

Significance

We report the feasibility study of time-resolved SAXS experiments on protein solution samples at the XFEL facility SACLA. Our experiments on standard samples demonstrate certain success relative to previous results obtained at synchrotron radiation facilities using an existing SFX system augmented with an additional helium path and newly developed analytical software. However, several issues were determined, likely due to the instrument configuration. These results are prepared to inform and advance future experimental methodologies and instrumentation development.

Introduction

Time-resolved serial femtosecond crystallography has enabled protein structural dynamic observation at the atomic level [1]. This technique has determined the dynamic structures of various photoreceptor proteins, including photoactive yellow

Corresponding authors: Nobutaka Shimizu, RIKEN SPring-8 Center, Sayo-gun, Hyogo 679-5148 Japan. ORCID iD: https://orcid.org/0000-0002-3636-1663, e-mail: nobutaka.shimizu.uj@riken.jp; Kensuke Tono, Japan Synchrotron Radiation Research Institute, Sayo-gun, Hyogo 679-5198, Japan. ORCID iD: https://orcid.org/0000-0003-1218-3759, e-mail: tono@spring8.or.jp; Eriko Nango, Institute of Multidisciplinary Research for Advanced Materials, Tohoku University, Sendai, Miyagi 980-8577, Japan. ORCID iD: https://orcid.org/0000-0001-9851-7355, e-mail: eriko.nango.c4@tohoku.ac.jp

protein, bacteriorhodopsin, photosystem II, phytochrome, and DNA photolyase [2–6]. However, the conformational changes of molecules in a crystal are limited because of crystal packing [7]. Spectroscopic analysis of bacteriorhodopsin in solution forms several intermediates, such as K-, L-, M-, N-, and O-states, upon light illumination, returning to the ground state [8]. Conversely, bacteriorhodopsin in the crystalline state, obtained in the lipidic cubic phase, reverts to the ground state without forming the N- and O-states while progressing similarly until the M state [9]. This difference is related to influences from crystal packing because the N- and O-states exhibit large conformational changes. Therefore, developing a measurement system to capture large structural alterations is indispensable. Thus, we aimed to establish a time-resolved small-angle X-ray scattering measurement system (TR-SAXS) using protein solution samples.

SAXS of protein solution samples (BioSAXS) is a technique for analyzing the molecular shape of proteins in solution [10]. It enables the external modulation of sample molecules more easily than the crystalline state and is not affected by crystal packing during conformational changes. This enables the observation of structural changes and intermolecular interactions accessible throughout the entire protein, although at a low resolution [11]. However, conducting TR measurements at synchrotron radiation facilities requires careful consideration of the radiation damage effects, which can frequently limit the structural information obtained and the time region in which measurements can be performed [12]. Conversely, no radiation damage effects were observed using 10-femtosecond pulse-width X-ray pulses from SACLA, enabling the measurement of highly accurate TR-SAXS profiles across a broad spatial scale. This would allow us to analyze not only the size changes but also the detailed shape changes in the molecules. We incorporated a helium path into a DAPHNIS system [13] that was originally developed for SFX experiments at the BL2 beamline at SACLA to construct a SAXS measurement system. We validated the system using ovalbumin, a standard sample in the SAXS field, in SAXS experiments under conditions where it was not mixed with other solutions. Additionally, we performed acid denaturation experiments on cytochrome c using a T-junction-type flow channel mixing system and observed changes in the scattering profiles upon denaturation (mix-and-inject-SAXS).

Materials and methods

Experimental procedure

The SAXS and mix-and-inject-SAXS measurements were performed at the BL2 of SACLA [14]. A helium path was integrated into the DAPHNIS system to prevent scattering intensity attenuation (Figure 1(a)). Additionally, the distance between the samples and the MPCCD-Phase III detector was set at 996 mm, calibrated with silver behenate powder. Helium gas was steadily supplied at a rate of 3 L/min to the sample chamber and 0.14 L/min to the helium path, ensuring

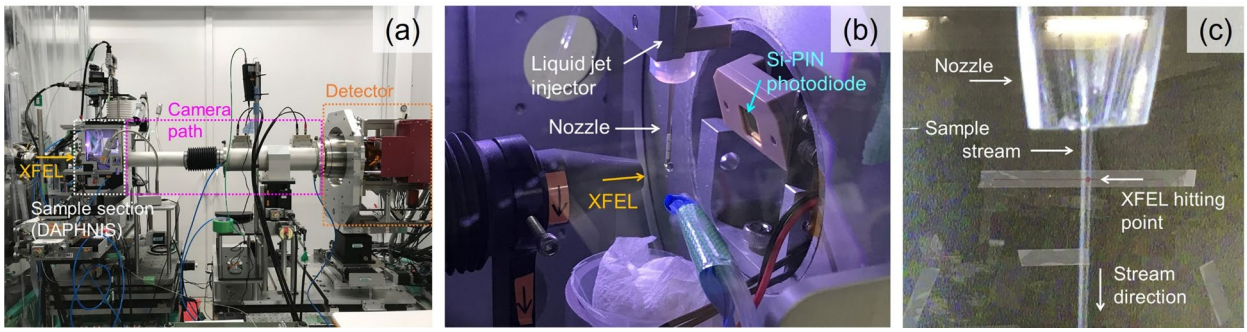

Figure 1 (a) SAXS measurement system developed for this project, illustrating the layout of the sample section, camera path, and detector. (b) Enlarged view of the sample section, highlighting the arrangement of the liquid jet injector, injector nozzle, and Si-PIN photodiode positioned on the wide-angle side directly behind the sample. (c) Close-up view of the sample stream area during the experiment, showing the injector nozzle, sample stream, XFEL hitting point, and the stream direction. The sample stream has an 83-μm diameter at a 1.0-mL/min pump flow rate.

that the helium concentrations were >96% in both the chamber and path during the measurements. A direct beam stopper with a Φ6-mm size was attached to a 50-μm thick polyimide film at the end of the helium path just before the detector. The range of scattering angle of 2θ measured with this configuration spanned from 0.17 to 3.3 degrees geometrically. Therefore, the measurement wavelength for the experiment was tuned to ~1.24 Å, enabling measurements of the scattering vector Q (Å^{-1}) within 0.013–0.280. The beam size was adjusted to 1.1 μm vertically and 1.3 μm horizontally (FWHM, 3 times average) through wire scanning at the sample position. A silicon pin (Si-PIN) photodiode (S3590, Hamamatsu) was positioned as an intensity monitor directly below the sample stream in the sample chamber to precisely align the narrow stream diameter with the even narrower XFEL beam (Figure 1(b)). This monitor detected strong parasitic scattering from

the sample stream observed outside the SAXS measurement angle range, helping in sample stream alignment with the beam position.

Albumin from hen egg white, ovalbumin (A7641, Sigma-Aldrich), and cytochrome c from equine heart (C7752, Sigma-Aldrich) were utilized as samples and dissolved in a buffer containing 10 mM HEPES pH 7, 100 mM NaCl. Ovalbumin and cytochrome c concentrations were adjusted to 10 and 15 mg/mL, respectively. Further dilutions were prepared in the same buffer to achieve concentrations of 5 and 2.5 mg/mL for ovalbumin. The sample solution was ejected from a 200-μm diameter nozzle for a liquid jet injector [13] to develop a stream guided by helium gas at a 0.2-L/min flow rate. The pump flow rate was set at 1.0 or 0.2 mL/min, causing stream diameters of 83 and 40 μm, respectively (Figure 1(c)). The SAXS image measurements were repeated for 3–10 runs, recording 3,000 images per run. As the repetition frequency of the pulse beam at SACLA is 30 Hz, it takes 100 s to measure 3,000 images. Hence, the amount of sample solution required for the measurement was 1.66 mL at 1.0 mL/min and 0.33 mL at 0.2 mL/min, respectively, and we prepared 5 mL of sample solution per concentration.

A pilot mix-and-inject-SAXS experiment with a T-junction two-channel mixing system [15] manipulated the reaction times by varying the pump flow rate and channel length from the mixing point to the intersection with the X-ray pulses. The pump flow rate was adjusted so that the total flow rate after mixing was either 1.0 or 0.2 mL/min, the same as the SAXS measurements without reactants. Two-channel lengths were used, and time stamp data were measured at 1.6 and 10 s for a 0.2-mL/min flow rate and at 0.3 and 2 s for a 1.0-mL/min flow rate. A 1 N HCl solution was used as a reactant solution to induce conformational changes in cytochrome c during acid denaturation. The flow rates of the two channels were set at 0.5 or 0.1 mL/min when mixing the sample solution and reactant in a 1:1 ratio, respectively. Only measurements with a total flow rate of 1.0 mL/min were performed at the time stamp of 0.3 s for a 1:3 ratio, and the sample and reactant flow rates were adjusted to 0.25 and 0.75 mL/min, respectively. The pH values of the mixed solutions recovered after the experiment were 0.4 for all four conditions in the 1:1 mixture and 0.2 for the 1:3 mixture. The amount of sample solution required for the measurement of 3,000 images per run was 0.83 mL at 0.5 mL/min and 0.16 mL at 0.1 mL/min for the 1:1 mixing, and 0.41 mL at 0.25 mL/min for the 1:3 mixing. We prepared 5 mL of sample solution for each time stamp measurement.

Software development and implementation

The acquired two-dimensional (2D) scattering intensity images need to be azimuthally averaged with the direct beam position at the center to generate a 1D SAXS profile. Therefore, we developed the software termed H2TC. Its purpose is to convert the HDF5 files produced by the MPCCD-Phase III detector into TIFF-format image files, thereby enabling processing with the existing SAXS analysis software. This command-based program is written in C++11, compiled with gcc 11.4, and verified for compatibility with both Ubuntu and Red Hat Enterprise Linux-based distributions, including Rocky Linux. Additionally, a graphical user interface (GUI) version for Windows 10 and 11 developed with Visual Studio 2019 is available (Figure 2). Essentially, H2TC converts all the data within a single HDF5 file into individual, integrated, or averaged TIFF files and outputs them respectively. The HDF5 file contains data tags with values, such as the incident beam intensity from SACLA; thus, the solution scattering intensities can be normalized using the beam intensity values. The XFEL beam intensity is constantly fluctuating; therefore, it is important not only to normalize the incident beam intensity but also to accurately generate a TIFF image using data within a specified intensity oscillation range. In addition, the image data generated by the MPCCD-Phase III detector contains abnormal pixel regions with high electrical noise

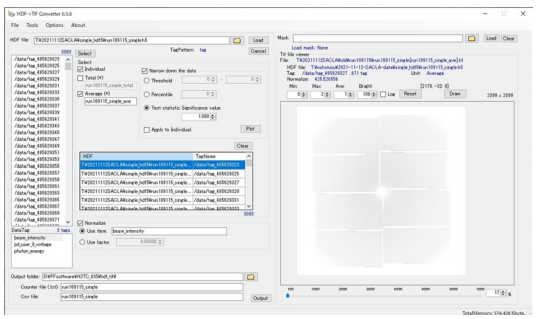

Figure 2 GUI version of H2TC software for Windows OS.

levels around the detector seams (GAP). These pixels must be determined and excluded from further processing. Consequently, a fundamental mask file needs to be created to exclude these abnormal pixels, and it is applied during data processing. H2TC can generate a histogram of the maximum intensity values recorded for each pixel with the mask in place, enabling us to monitor the status of the data. Additionally, it provides the capability to exclude data that deviates

from the specified threshold from further processing. These threshold values can be user-defined, based on percentiles, or identified using a test statistic, z, as shown in the following equation. The data are omitted from the processing if z is outside the threshold range.

$$z = \left| \frac{I_{pixel} - I_{average}}{Standard\ deviation} \right|$$

In this process, the averaged TIFF data was established from 3,000 images while applying both masks to eliminate inappropriate pixel regions and the threshold range based on z-values. The intensity values recorded in pixels were normalized with the incident beam intensity. The resulting TIFF files were processed by incorporating the specification of the MPCCD-Phase III into the detector configuration file of the SAngler software [16]. SAngler performed the conversion of the 2D SAXS intensity into 1D through azimuthal averaging and, finally, the SAXS profile calculation for the sample molecules by buffer profile subtraction. Data for the same sample obtained from multiple runs were averaged to generate a single scattering profile.

Results and discussion

Data reduction process

Figure 3(a) illustrates the TIFF data averaged from 3,000 images collected in a single run. Figure 3(b-c) presents the results of plotting the maximum intensity value from these 3,000 images. The values demonstrate significant fluctuations due to factors like electrical noise without the mask. However, with the mask applied, the range of variation in the values is almost equivalent to the fluctuation in the XFEL beam intensity. Both Figures 3(b-c) set the z-value threshold of 1.5, and data falling outside this threshold were excluded from subsequent processing. These results indicate the necessity of applying the mask and the threshold for proper processing.

Figure 4 illustrates the 1D scattering intensity profiles azimuthally averaged from the TIFF files using SAngler. The scattering intensity varies with the sample concentration. However, weak scattering intensities were found around the

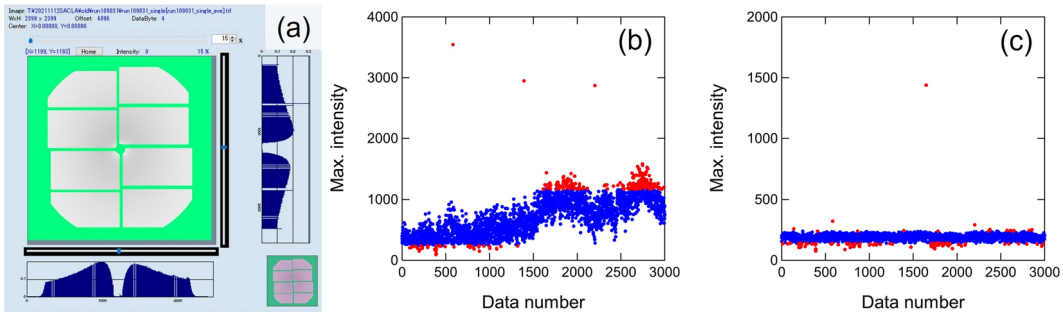

Figure 3 (a) The results of measuring ovalbumin at a 10-mg/mL concentration with a 1-mL/min pump flow rate. Data from one run were averaged and converted to a TIFF image, which was normalized by the incident beam intensity. Masked areas are indicated by the light green in SAngler. (b-c) The maximum intensity values for each of the 3,000 images measured in one run were analyzed under (b) unmasked and (c) masked conditions and plotted, respectively. The blue and red dots represent data with z-values of ≤1.5 and >1.5, respectively.

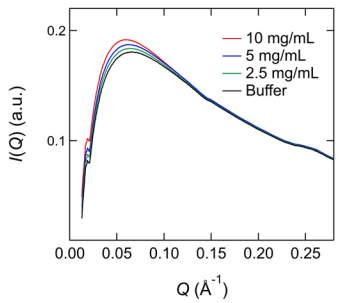

Figure 4 The azimuthal averaged profiles for ovalbumin with concentrations of 10, 5, and 2.5 mg/mL and the buffer. All data were measured at a 1.0-mL/min pump flow rate.

direct beam stopper, causing a concave shape in the scattering intensity profile around the small-angle region. This phenomenon indicates that something attenuates the scattering intensity near the direct beam. We assume that the water solution evaporates by XFEL pulses and attenuates the scattering intensity near the direct beam upon XFEL impact since the substitution rate of helium gas in the path was sufficient.

SAXS measurements

Figure 5 presents the results of the SAXS measurements of ovalbumin. The scattering intensities at 1.0 mL/min are higher than those at 0.2 mL/min, and the signal-to-noise ratio (S/N) of the data appears better at 1.0 mL/min, compared with data of 2.5 mg/mL due to differences in the sample stream diameter depending on the flow rate. SAXS beamline at SR facilities typically measures ovalbumin at concentrations of approximately 1–5 mg/mL. However, to obtain data with a comparable S/N ratio, it was necessary to measure at a slightly higher concentration in this experiment. Hence, increasing the number of measurements (i.e., the number of runs) would simply be necessary to obtain data with sufficient S/N at lower concentrations in XFEL measurements. Additionally, a larger sample stream diameter to increase the scattering volume would be effective for improving the S/N, although the total volume of the sample may need to be considered. Conversely, Figure 4 illustrates the S/N of the data is presumably affected by the issue of the scattering intensity attenuation in the small-angle region. The radius of gyration (R_g) and forward scattering intensity ($I(0)$), derived from Guinier analysis (Figure 5(c)), are summarized in Table 1. Since the R_g values exhibited a concentration dependence, extrapolation to zero concentration was performed, yielding values of 26.4 (±0.3) Å for 1.0 mL/min and 26.9 (±0.5) Å for 0.2 mL/min, respectively. These values are comparable to those obtained at SR facilities [17]. Therefore, it is thought that the observed intensity attenuation in the small-angle region does not significantly affect the shape of the SAXS profile in this region.

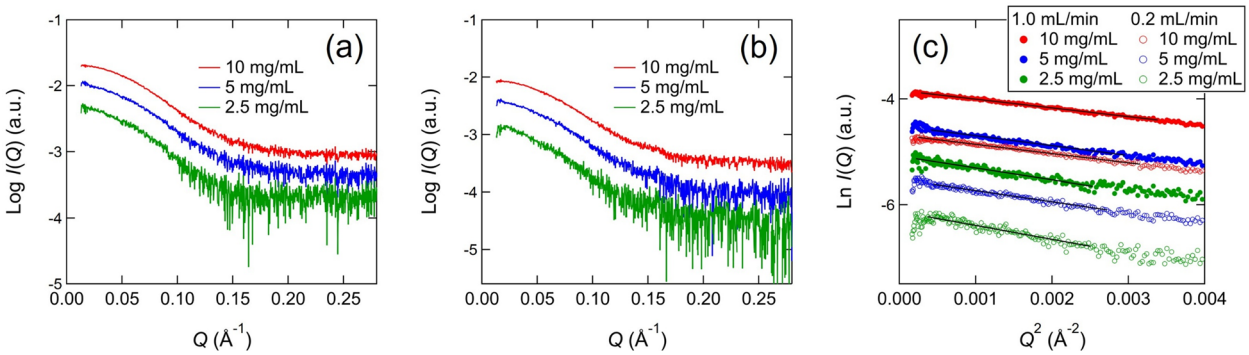

Figure 5 SAXS profiles for ovalbumin with concentrations of 10, 5, and 2.5 mg/mL. These measurements were conducted at a pump flow rate of (a) 1.0 mL/min and (b) 0.2 mL/min, respectively. (c) Guinier plots for all six profiles. The lines show the results of the linear approximation based on Guinier analysis ($QR_g < 1.3$).

Table 1 R_g and $I(0)$ values obtained from Guinier analysis in Figure 5(c)

	1.0 mL/min			0.2 mL/min	
	10 mg/mL	5 mg/mL	2.5 mg/mL	10 mg/mL	5 mg/mL
R_g (Å)	22.4 (0.1)	24.0 (0.2)	25.9 (0.3)	23.0 (0.1)	24.9 (0.3)
$I(0)$ (a.u.)	0.0216 (6.6E-5)	0.0111 (7.7E-5)	0.0062 (6.1E-5)	0.0093 (4.0E-5)	0.0040 (3.3E-5)

The values in parentheses show the error.

Mix-and-inject-SAXS measurements

Figure 6 illustrates the pilot study on the acid denaturation experiment of cytochrome c. The dimensionless Kratky plot, normalized by R_g and $I(0)$ that were obtained from Guinier analysis (Table 2), provides a qualitative assessment of the protein folding status that is independent of the molecular size and the scattering intensity [18]. A bell-shaped peak with a height of 3/e appears at $QR_g = \sqrt{3}$ for rigid globular proteins in this plot. As denaturation progresses, the profile changes, with the peak shifting outward and gradually disappearing, revealing a plateau region. Eventually, the profile transitions into a continuously and monotonically increasing pattern in complete denaturation. For 1:1 mixing, the scattering profiles for the native state at pH 7.0 were consistent, forming a bell-shaped peak, regardless of the differences in the pump flow rates or the diameters of the sample stream. The profile at 0.3 s after mixing with 1 N HCl demonstrated a peak shifting

to the high-angle side and an upturn in the entire profile. Furthermore, the peak shifted further to the high-angle side, a plateau region appeared, and the profile at the higher-angle side turned to a further increase at 1.6, 2.0, and 10 s. Cytochrome c has been extensively studied using SAXS to investigate protein folding mechanisms, with structural changes induced by acid denaturation observed under both static and time-resolved conditions [19,20]. Reported R_g values include ~13.5 Å in the native state, ~17–20 Å for a folding intermediate, ~24 Å for the acid-denatured state at pH 2, and ~32 Å for the fully denatured state in 4 M guanidine hydrochloride. In this experiment, the R_g value in the native state was slightly smaller but appeared comparable to previously reported values, as it was not derived through extrapolation to zero concentration. At 0.3 seconds, the R_g values in the 1:1 and 1:3 mixtures were 18.0 Å, consistent with those characteristic of a folding intermediate. At later time stamps, the values exceeded those observed for acid denaturation at pH 2. Given that the post-mixing pH was significantly lower than pH 2, regardless of the mixing ratio, it is likely that acid-induced structural changes progressed gradually over time. Conversely, in the 1:1 mixture, the degree of structural change observed at 1.6 and 2.0 seconds was reversed. Additionally, in the 1:3 mixture, the extent of change at 0.3 seconds was smaller than that observed in the 1:1 mixture at the same reaction time. The mixing efficiency may have been compromised at higher total flow rates due to the capacity limitations of the mixer. However, further investigation is necessary to elucidate the factors underlying these observations, such as simulating the pH at the beam hit point or directly measuring it if feasible.

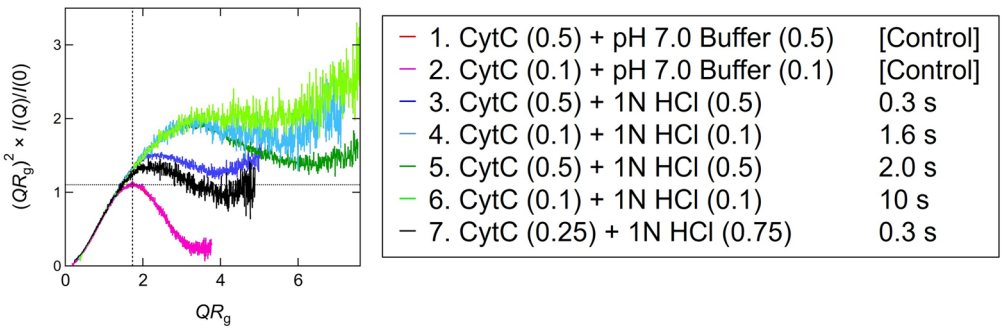

Figure 6 Dimensionless Kratky plot of SAXS profiles for cytochrome c (CytC). The values in parentheses indicate each flow rate of the pump before mixing.

Table 2 R_g and I (0) values obtained from Guinier analysis. Sample numbers are consistent with Figure 6

Sample No.	1	2	3	4	5	6
R_g (Å)	12.7 (0.1)	12.8 (0.1)	18 (0.1)	25.7 (0.1)	26.9 (0.1)	27.1 (0.1)
I (0) (a.u.)	0.0082 (1.1E-5)	0.0027 (6.8E-6)	0.0078 (1.7E-5)	0.0042 (1.8E-5)	0.0119 (2.5E-5)	0.0069 (2.7E-5)

The values in parentheses show the errors.

Conclusion

We developed a SAXS experimental system at SACLA BL2 and conducted a pilot study of the mix-and-inject SAXS. However, improvements in the S/N ratio across the dataset are required, particularly to address the reduced scattering intensity in the small-angle region near the direct beam. We investigated the effect of the sample flow diameter and flow rate under various conditions by replacing the injector nozzle diameter to 100 and 300 μm, in addition to the 200 μm used in this experiment, and varying the pump flow rate up to a maximum of 14.2 ml/min. Additionally, we experimented with an enlarged beam size of 9.5 μm (vertical) × 9.5 μm (horizontal). Furthermore, we attempted to enhance the helium gas concentration by increasing the flow velocity within the helium path. However, we were unable to resolve this phenomenon in these modifications fundamentally. An aspirator nozzle was installed adjacent to the irradiation point to remove any vapors generated by the XFEL irradiation of the sample, but this countermeasure also proved ineffective. Given that similar pilot experiments at other XFEL beamlines have been performed under vacuum conditions from the sample environment to the detector [21], it is crucial not only to investigate the underlying causes of this challenge but also to explore system modifications that would enable experiments under comparable vacuum conditions. Additionally, electrical noise fluctuated randomly during the measurements, rather than being confined to specific pixels. Data affected

by unmasked abnormal pixels caused by this noise can be excluded during subsequent processing by applying a histogram analysis threshold based on the maximum intensity value. However, real-time masking or alternative approaches will be established for future experiments.

Building upon our experience with SFX at SACLA, we developed an experimental setup utilizing a liquid jet system. In recent years, a time-resolved SAXS system employing a microfluidic device has been developed for SR beamlines [22-24], which are based on a similar fundamental concept. In these measurements, the time stamp is determined by the pump flow rate and volume from the mixing point, necessitating flow rate adjustments according to the measurement time scale. Consequently, high-flow rate measurements inevitably resulted in increased sample consumption. There is no fundamental distinction between SR and XFEL experiments in this regard. However, SACLA's high-intensity X-ray pulses with a pulse duration of 10 femtoseconds enable the acquisition of SAXS images free from radiation damage. The liquid jet system is especially well suited for XFEL-based measurements and is expected to provide high-precision time-resolved data from more dilute solutions than those typically used for SR beamline analysis. Nonetheless, because of the aforementioned instrumental challenges, we were unable to fully validate this advantage in the present experiment. Furthermore, in this study, the time stamp was controlled by adjusting the tube length from the mixing point; however, this approach makes tube replacement a rate-limiting step when modifying the measurement time. To overcome this limitation, it is necessary to enhance the sample delivery system by incorporating an automated mechanism that allows adjustment of the X-ray pulse irradiation point and distance from the mixing point, which is similar to the SR microfluidic device. We will continue to refine the system to establish a measurement environment with even greater precision while reducing the sample amount required.

From another perspective, calibrating the scattering intensity to an absolute scale in the SAXS measurements using XFELs presents significant challenges and has not been performed in this study or similar reported research [21]. In SR experiments, such calibration is standard to comply with the SAXS publication guidelines [25]. The X-ray transmittance through the sample required for this calibration is typically determined by measuring the transmitted intensity with a photodiode embedded in a direct beam stopper. However, XFEL's extremely high-intensity pulse beam would damage the photodiode, rendering this approach impractical. Moreover, as observed in this experiment and previous studies, the intense XFEL pulse beam causes the sample solution to instantaneously evaporate after scattering, making it difficult to accurately measure the transmitted intensity, even if a small ion chamber or similar device is placed directly below the sample. To achieve compliance with the guidelines, it will be necessary to develop a suitable calibration method through the collaboration of engineers and researchers involved in various scientific fields.

Conflict of interest

All authors declare no conflicts of interest.

Author contributions

N.S., K.T., S.I., and E.N. designed this research and conceived the project. K.T. designed and constructed instruments for the SAXS experiments. N.S., F.L., T.T., and E.N. conducted the SAXS experiments. N.S., F.L., and E.N. analyzed the data for this manuscript. K.Y. and N.S. developed the new software H2TC and advanced the existing software SAngler. All the members discussed the results of the experiment. N.S., F.L., and E.N. wrote the paper.

Data availability

The evidence data generated and/or analyzed during the current study are available from the corresponding author upon reasonable request.

Acknowledgments

We thank Dr. Shigeki Owada (Japan Synchrotron Radiation Research Institute) and Prof. Takehiko Tosha (University of Hyogo and RIKEN SPring-8 Center) for their experimental support at SACLA. We also thank Mr. Kazunori Hata (Engineering Team, RIKEN SPring-8 Center) for his construction of the SAXS instruments. The XFEL experiments were performed at the BL2A of SACLA with the approval of the Japan Synchrotron Radiation Research Institute (Proposal No. 2019B8043, 2020A8026, and 2021B8062). This study was supported by JSPS KAKENHI Grant Number JP19H05781. This study was partially supported by the Research Support Project for Life Science and Drug Discovery [Basis for Supporting Innovative Drug Discovery and Life Science Research (BINDS)] from AMED under Grant Numbers JP21am0101070, JP21am0101071, and JP22ama121001.

References

[1] Fadini, A., Hutchison, C. D., Morozov, D., Chang, J., Maghlaoui, K., Perrett, S., et al. Serial femtosecond crystallography reveals that photoactivation in a fluorescent protein proceeds via the hula twist mechanism. J. Am. Chem. Soc. 145, 15796-15808 (2023). https://doi.org/10.1021/jacs.3c02313

[2] Pande, K., Hutchison, C. D., Groenhof, G., Aquila, A., Robinson, J. S., Tenboer, J., et al. Femtosecond structural dynamics drives the trans/cis isomerization in photoactive yellow protein. Science 352, 725-729 (2016). https://doi.org/10.1126/science.aad5081

[3] Nogly, P., Weinert, T., James, D., Carbajo, S., Ozerov, D., Furrer, A., et al. Retinal isomerization in bacteriorhodopsin captured by a femtosecond x-ray laser. Science 361, eaat0094 (2018). https://doi.org/10.1126/science.aat0094

[4] Suga, M., Akita, F., Sugahara, M., Kubo, M., Nakajima, Y., Nakane, T., et al. Light-induced structural changes and the site of O=O bond formation in PSII caught by XFEL. Nature 543, 131-135 (2017). https://doi.org/10.1038/nature21400

[5] Edlund, P., Takala, H., Claesson, E., Henry, L., Dods, R., Lehtivuori, H., et al. The room temperature crystal structure of a bacterial phytochrome determined by serial femtosecond crystallography. Sci. Rep. 6, 35279 (2016). https://doi.org/10.1038/srep35279

[6] Maestre-Reyna, M., Wang, P.-H., Nango, E., Hosokawa, Y., Saft, M., Furrer, A., et al. Visualizing the DNA repair process by a photolyase at atomic resolution, Science 382, eadd7795 (2023). https://doi.org/10.1126/science.add7795

[7] Efremov, R., Gordeliy, V. I., Heberle, J., Buldt, G. Time-resolved microspectroscopy on a single crystal of bacteriorhodopsin reveals lattice-induced differences in the photocycle kinetics. Biophys. J. 91, 1441-1451 (2006). https://doi.org/10.1529/biophysj.106.083345

[8] Ernst, O. P., Lodowski, D. T., Elstner, M., Hegemann, P., Brown, L. S., Kandori H. Microbial and animal rhodopsins: structures, functions, and molecular mechanisms. Chem. Rev. 114, 126-163 (2014). https://doi.org/10.1021/cr4003769

[9] Nango, E., Royant, A., Kubo, M., Nakane, T., Wickstrand, C., Kimura, T., et al. A three-dimensional movie of structural changes in bacteriorhodopsin, Science 354, 1552-1557 (2016). https://doi.org/10.1126/science.aah3497

[10] Jiang, X., Ogawa, T., Yonezawa, K., Shimizu, N., Ichinose, S., Uchihashi, T., et al. The two-step cargo recognition mechanism of heterotrimeric kinesin. EMBO Rep. 24, e56864 (2023). https://doi.org/10.15252/embr.202356864

[11] Takahashi, D., Yonezawa, K., Okizaki, Y., Caaveiro, J. M. M., Ueda, T., Shimada, A., et al. Ca^{2+}-induced structural changes and intramolecular interactions in N-terminal region of diacylglycerol kinase alpha. Protein. Sci. 31, e4365 (2022). https://doi.org/10.1002/pro.4365

[12] Berntsson, O., Terry, A. E., Plivelic, T. S. A setup for millisecond time-resolved X-ray solution scattering experiments at the CoSAXS beamline at the MAX IV Laboratory. J. Synchrotron. Radiat. 29, 555-562 (2022). https://doi.org/10.1107/S1600577522000996

[13] Tono, K., Nango, E., Sugahara, M., Song, C., Park, J., Tanaka, T., et al. Diverse application platform for hard X-ray diffraction in SACLA (DAPHNIS): Application to serial protein crystallography using an X-ray free-electron laser. J. Synchrotron. Radiat. 22, 532-537 (2015). https://doi.org/10.1107/S1600577515004464

[14] Tono, K., Hara, T., Yabashi, M., Tanaka, H. Multiple-beamline operation of SACLA. J. Synchrotron. Radiat. 26, 595-602 (2019). https://doi.org/10.1107/S1600577519001607

[15] Stagno, J. R., Liu, Y., Bhandari, Y. R., Conrad, C. E., Panja, S., Swain, M., et al. Structures of riboswitch RNA reaction states by mix-and-inject XFEL serial crystallography. Nature 541, 242-246 (2017). https://doi.org/10.1038/nature20599

[16] Shimizu, N., Yatabe, K., Nagatani, Y., Saijyo, S., Kosuge, T., Igarashi, N. Software development for analysis of small-angle X-ray scattering data. AIP Conf. Proc. 1741, 050017 (2016). https://doi.org/10.1063/1.4952937

[17] Mylonas, E., Svergun, D. I. Accuracy of molecular mass determination of proteins in solution by small-angle X-ray scattering. J. Appl. Cryst. 40, s245-s249 (2007). https://doi.org/10.1107/S002188980700252X

[18] Receveur-Brechot, V., Durand, D. How random are intrinsically disordered proteins? A small angle scattering perspective. Curr. Protein Pept. Sci. 13, 55-75 (2012). https://doi.org/10.2174/138920312799277901

[19] Kataoka, M., Hagihara, Y., Mihara, K., Goto, Y. Molten globule of cytochrome c studied by small angle X-ray scattering. J. Mol. Biol. 229, 591-596 (1993). https://doi.org/10.1006/jmbi.1993.1064

[20] Akiyama, S., Takahashi, S., Kimura, T., Ishimori, K., Morishima, I., Nishikawa, Y., et al. Conformational landscape of cytochrome c folding studied by microsecond-resolved small-angle x-ray scattering, Proc. Natl. Acad. Sci. U.S.A. 99, 1329-1334 (2002). https://doi.org/10.1073/pnas.012458999

[21] Blanchet, C. E., Round, A., Mertens, H. D. T., Ayyer, K., Graewert, M., Awel, S., et al. Form factor determination of biological molecules with X-ray free electron laser small-angle scattering (XFEL-SAS). Commun. Biol. 6, 1057

(2023). https://doi.org/10.1038/s42003-023-05416-7
[22] Graceffa, R., Nobrega, R. P., Barrea, R. A., Kathuria, S. V., Chakravarthy, S., Bilsel, O., et al. Sub-millisecond time-resolved SAXS using a continuous-flow mixer and X-ray microbeam. J. Synchrotron Radiat. 20, 820-825 (2013). https://doi.org/10.1107/S0909049513021833
[23] Martin, E. W., Harmon, T. S., Hopkins, J. B., Chakravarthy, S., Incicco, J. J., Schuck, P., et al. A multi-step nucleation process determines the kinetics of prion-like domain phase separation. Nat. Commun. 12, 4513 (2021). https://doi.org/10.1038/s41467-021-24727-z
[24] Maeki, M., Kimura, N., Okada, Y., Shimizu, K., Shibata, K., Miyazaki, Y., et al. Understanding the effects of ethanol on the liposome bilayer structure using microfluidic-based time-resolved small-angle X-ray scattering and molecular dynamics simulations. Nanoscale Adv. 6, 2166-2176 (2024). https://doi.org/10.1039/D3NA01073B
[25] Trewhella, J., Duff, A. P., Durand, D., Gabel, F., Guss, J. M., Hendrickson, W. A., et al. 2017 publication guidelines for structural modelling of small-angle scattering data from biomolecules in solution: an update. Acta Cryst. D73, 710-728 (2017). https://doi.org/10.1107/S2059798317011597